Satellite Tobacco Mosaic Virus: Revealing Environmental Drivers of Capsid and Nucleocapsid Stability using High-Resolution Simulations

Marharyta Blazhynska,* Olivier Adjoua, Zoe Vetter, Louis Lagardère, and Jean-Philip Piquemal*

LCT, Sorbonne Université, UMR 7616 CNRS, 75005 Paris, France

E-mail: marharyta.blazhynska@sorbonne-universite.fr; jean-philip.piquemal@sorbonne-universite.fr

Abstract

Satellite tobacco mosaic virus (STMV) is a model system for studying viral assembly and stability due to its architecture: a single-stranded RNA genome enclosed in an icosahedral capsid. Coupling a polarizable force-field to enhanced sampling, we explored at high-resolution the long-timescale structural dynamics of a complete ∼1M-atom STMV. RNA-free capsids exhibit remarkable stability at physiological salt concentrations, suggesting an evolutionary adaptation for capsid reuse during the viral life cycle. This observation challenges the notion that empty capsids are exclusively products of abortive assembly, positioning them instead as functional intermediates in viral reproduction. Additionally, RNA encapsidation creates electrostatic dependencies that magnesium ions mitigate, stabilizing both RNA and capsid through long-residence-time interactions with phosphate groups. Chloride ions further influence capsid permeability by modulating salt-bridge disruptions and interprotomeric interactions, with these effects being pH-dependent: enhanced at pH < 7, preserving nucleocapsid integrity, or weakened at pH = 7, facilitating disassembly and RNA release.

The satellite tobacco mosaic virus (STMV), a single-stranded RNA (ssRNA) virus with a T=1 icosahedral structure of approximately 170 Å in diameter[1,2], relies on the tobacco mosaic virus (TMV) as a helper for its replication and has been a subject of extensive research since its discovery by Dodds et al. in 1987[3–6]. Considerable research efforts have been devoted to elucidating the mechanisms underlying its viral assembly and stability, focusing on the dynamics of the viral protein shell, known as capsid. Despite significant progress, the structural behavior of the capsid, both in the presence and absence of single-stranded RNA (ssRNA), remains a topic of ongoing debate[1,2,7–10].

Experimental studies from the early 1990s on viruses analogous to STMV suggested that, while nucleic acids interact specifically with their protein coats, this interaction may not be essential for capsid assembly, as nucleic acid-free capsids (i.e. "empty" capsids) were found to exhibit remarkable structural stability that are independent of the presence of the viral genome[5,11–17]. For instance, Chen et al.[15] demonstrated that comoviruses can self-assemble *in vivo*, driven by strong protein-protein interactions, with RNA subsequently encapsulated by recognizing the pre-assembled icosahedral scaffold. Extending these insights, a recent *in vitro* study by Sivanandam et al.[18] showed that STMV capsid proteins can reassemble around newly synthesized RNA molecules without requiring *de novo* protein synthesis. These findings underline the robustness of capsid structures and suggest that empty capsids may arise not only as abortive assembly products[19,20] but also as functional intermediates, playing an essential role in the viral life cycle. In contrast, a pioneering all-atom classical molecular dynamics (MD) computational study, conducted by Klaus Schulten's group[21,22], revealed that empty capsids, while permeable, are prone to collapse within a 10-nanosecond simulation timescale. Their research focused on two scenarios: (i) the STMV capsid in the presence of ssRNA neutralized by magnesium chloride, $MgCl_2$, and (ii) the STMV empty capsid neutralized by chloride ions, Cl^-. The outlines of their study while underscore the crucial role of RNA in stabilizing its protein coat structure, show that the capsid structural integrity is heavily dependent of the RNA binding, particularly in the presence of Mg^{2+} ions.

The observed discrepancies between computational and experimental studies prompted us to

revisit the stability of STMV capsids. Aiming to provide an accurate representation of interactions, we reproduced the study cases examined by Schulten's group, leveraging the advanced polarizable AMOEBA force field[23–25]. We performed two sets of independent STMV simulations and introduced four additional biologically relevant scenarios reflecting the different environmental conditions encountered throughout the viral life cycle[26]. Plant cellular environments are known to exhibit a range of pH values, with the cytoplasm maintaining a near-neutral pH of approximately 7, while certain organelles, such as vacuoles or vesicular compartments, are more acidic[27–33]. To investigate how pH and ionic strength modulate the capsid stability, towards drug delivery where capsid behavior under varying conditions is critical, we included the following scenarios: (i) an empty STMV capsid at physiological NaCl concentration (i.e., 0.15 M) to evaluate the capsid stability under cytoplasmic-like conditions (pH=7); (ii) a STMV nucleocapsid in physiological concentration[34], providing a baseline for assessing RNA impact on capsid stability in absence of Mg^{2+}; (iii) a STMV nucleocapsid in a physiological NaCl concentration supplemented with Mg^{2+}, to approximate the STMV behavior under typical physiological environments[35,36] and (iv) a STMV nucleocapsid in 0.5 M NaCl with Mg^{2+} ions at pH=5, representing the plant vesicular compartments[28,29,32,33]. The details of the studied STMV particles, including the number of water molecules, ions, and total atom count, are provided in Table 1. In total, a cumulative of 700 nanoseconds of conventional MD simulations were performed to explore the STMV structural dynamics at the atomic level. To deepen the investigation of the observed STMV swelling and compaction as a response to the environmental conditions, we additionally employed 300-ns well-tempered metadynamics (WTMetaD)[37] simulations using the capsid radius of gyration (r_{gyr}) as the collective variable (CV).

Our findings reveal contrasting behaviors between the studied STMV particles highlighting the impact of the chosen environment. The empty capsid, when neutralized, undergoes slight swelling but stabilizes in physiological ionic concentrations, highlighting its potential to exist independently of genome. Besides, new insights into the dual role of ions in stabilizing the capsid and regulating its permeability were presented. At physiological pH, Mg^{2+} ions reinforce capsid cohesion and

Table 1. Summary of studied STMV particles.

№	STMV particle	$N_{\text{atoms}}^{\text{tot}}$	N_{water}	$N_{\text{Mg}^{2+}}$	$N_{\text{Na}^{+}}$	$N_{\text{Cl}^{-}}$
1	Capsid neutralized, pH=7	1034475	299405	–	–	299
2	Capsid in C(NaCl)=0.15M, pH=7	457162	106766	–	302	601
3	Nucleocapsid in C(NaCl)=0.15M, pH=7	790181	207413	–	1066	586
4	Nucleocapsid neutralized $MgCl_2$, pH=7	1066618	299854	474	–	296
5	Nucleocapsid C(NaCl)=0.15M, Mg^{2+}, pH=7	1063260	298173	474	841	1140
6	Nucleocapsid C(NaCl)=0.5M, Mg^{2+}, pH=5	913508	247268	474	2358	2586

RNA stability through long-residence interactions with phosphate groups, while Cl^- ions dynamically modulate salt-bridge disruption and interprotomeric interactions. At acidic pH, an excess of positively charged ions promotes nucleocapsid integrity, suggesting its evolutionary adaptation to the vesicular environment of plant hosts. Our findings not only advance the understanding of STMV dynamics but also highlight potential applications in antiviral strategies.

Results and Discussion

Capsid Stability and Dynamics

Figure 1 illustrates the structural organization of the STMV capsid and its interactions with encapsidated RNA. The capsid, composed of 60 identical protomers (Fig.1D), forming its icosahedral symmetry. Such geometric arrangement inherently creates structural voids — interstitial spaces between protomers[28,38](Fig.1C). Within each protomer (Fig.1D), charged residues (i.e., ARG, LYS, ASP, and GLU) play a key role in both interprotomeric stability and RNA binding.

To gain deeper insights into the structural organization and stability of the STMV capsid, we first explored the role of RNA in capsid stability (Fig.1E)[39–41]. Across nucleocapsid-related STMV particles (i.e., №3-№6, Table 1), we analyzed the hydrogen bonding network between the protein shell and the RNA phosphate backbone (see Fig.S2 in Supplementary Information (SI)). Amino-phosphodiester interactions, specifically between the amino groups of the side chains of the capsid protein and the oxygen atoms of the RNA phosphodiester backbone, dominate the interaction landscape, accounting for approximately 30% of the total capsid-RNA hydrogen bonds. Importantly,

the strength and prevalence of RNA-capsid interactions varied across STMV particles, reflecting the impact of ionic conditions on capsid stability. In №3, the absence of Mg^{2+} limits charge screening, leading to a greater reliance on direct hydrogen bonding between RNA and the capsid. Conversely, in №6, an excess of ions may introduce electrostatic over-shielding, requiring RNA to maintain stability through phosphodiester-mediated contacts. Such dynamic modulation of RNA-protein interactions suggests an evolutionary adaptation of STMV to fluctuating host ionic conditions, ensuring structural integrity under varying electrostatic environments. Beyond amino-phosphodiester interactions, capsid-ribose and capsid-base hydrogen bonds, though less frequent (10%), contribute to the overall stabilization of the RNA-protein interface. In №4, interactions with adenine bases are less pronounced yet still present, indicating a structural reorganization of the capsid in response to environmental conditions. These findings underscore the delicate balance of electrostatic interactions between ions, RNA, and the capsid, emphasizing the pivotal role of RNA in maintaining viral stability (Fig.1B).

To further evaluate the structural dynamics of the capsid, we analyzed the root mean square deviation (RMSD), radius of gyration (r_{gyr}), and root mean square fluctuation (RMSF) of Cα atoms during individual 100–ns conventional MD simulations (Fig.2A-C). While RMSD and r_{gyr} provide insights into global structural changes, RMSF highlights localized fluctuations in the capsid, enabling a comprehensive assessment of capsid stability and dynamics.

The resulting profiles reveal distinct structural dynamics behaviors among the STMV particles, highlighting the influence of environmental conditions on the capsid. For №1 (neutralized capsid), RMSD reaches $\sim$9 Å by the end of 100 ns, indicating significant protein coat reorganization during the simulation. In contrast to the collapse observed in prior MD studies by Freddolino et al.[21], our simulations demonstrate that the capsid retains its overall structure, albeit undergoing substantial rearrangements in the absence of stabilizing ionic concentrations (Fig.2A, №1). Remarkably, the inclusion of physiological NaCl (№2, RMSD $\sim$3 Å) stabilizes the empty capsid, preserving its structural integrity and highlighting the essential role of positively-charged monovalent ions (i.e.,Na^{+}) in maintaining capsid symmetry. However, for nucleocapsid №3, the presence

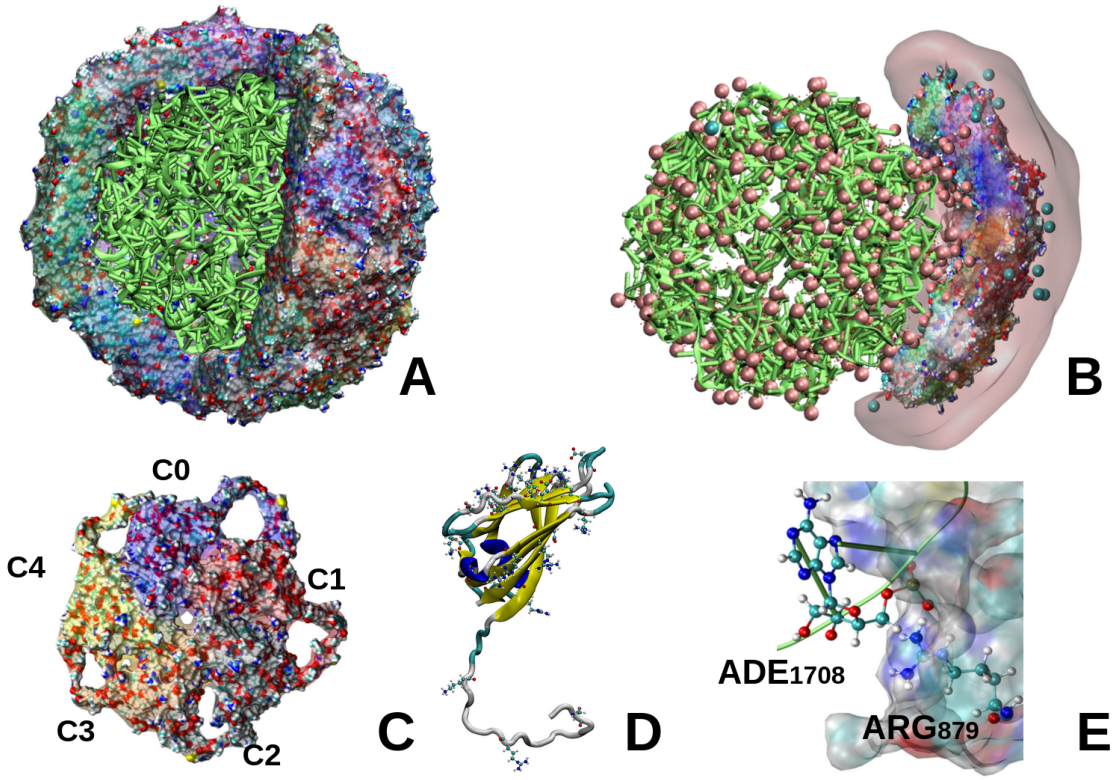

Figure 1. Structural features of STMV capsid and its interactions with RNA visualized by means of Visual Molecular Dynamics sofware (VMD)[42]. (A) Molecular surface representation of the STMV capsid, colored by electrostatic potential[43], with the encapsidated RNA shown shown in green. (B) Capsid–RNA complex with surrounding ions (Mg^{2+} and Cl^{-} in pink and teal spheres, respectively). (C) Surface representation of a pentameric capsid unit (C0–C4). (D) A representative capsid identical protomer unit with visualized charged residues of ASP, GLU, ARG, and LYS. β-sheets, α-helices, loops and turns are depicted in yellow, blue, white and cyan, respectively. (E) Close-up of a RNA–protein interaction site, showcasing the most frequent H-bonding interactions occuring between the phosphodiester of RNA and protein sidechain on the example of ADE_{1708} and ARG_{879}.

of only physiological salt concentration is insufficient for STMV stabilization. RNA alone does not provide a robust scaffold for capsid stability under physiological conditions, emphasizing the indispensable role of divalent ions in maintaining both RNA and capsid integrity[44–47]. №4 and №5 further underscore the critical role of divalent ions (e.g., Mg^{2+}) in stabilizing the RNA, which in turn influences the capsid structure through ionic interactions. Besides, №5, the nucleocapsid at pH=7 with physiological NaCl concentration in the presence of Mg^{2+}, exhibits increased fluctuations in the capsid structure, suggesting that under neutral physiological conditions, an imbalance

between charge repulsion and shielding occurs, leading to greater flexibility and reduced structural rigidity of the capsid (Fig.2).

It should be noted that none of the studied STMV particles reached a plateau in either the RMSD or r_{gyr} by the end of the 100-ns simulations, underscoring the highly dynamic nature of the capsid and its sensitivity to ionic conditions. The most significant changes were observed in the r_{gyr} profiles, with notable shifts in capsid compactness and organization. The RMSF profiles (Fig.2C) further reveal regions of elevated flexibility, which may contribute to the capsid adaptive response to environmental changes. Such dynamical responses are reflected in the final capsid structures (Fig.2E), which exhibit distinct differences in compactness and symmetry across the various simulation conditions. №1 and №3 show the greatest degree of asymmetry, while №2, №4-6 remain relatively stable, emphasizing the stabilizing effects of monovalent and divalent ions under different ionic conditions.

Enhanced Sampling along Capsid Gyration Radius

The pronounced fluctuations in the radius of gyration (r_{gyr}) dynamics observed during the 100-ns simulations (Fig.2B) highlighted the limitations of conventional molecular dynamics in evaluating stable capsid profiles. To investigate the free-energy landscape associated with the structural organization of the capsid under different environmental conditions, we turned to the enhanced sampling approach, notably well-tempered metadynamics (WTMetaD)[37,48,49] that allowed us to evaluate the potential of mean force (PMF) profiles for all STMV particles, using r_{gyr} as the collective variable (CV) (Fig.2D).

The PMF profiles revealed distinct behaviors depending on the presence of RNA and ionic conditions. Among the empty capsids, №2 exhibited one of the narrowest PMF profiles, with a free-energy minimum at ∼69 Å, indicating a compact and stable capsid structure with notable resistance to expansion. In contrast, №1 displayed a broader PMF minimum along with a broader distribution (see Fig.S5 for the corresponding histograms of sampled states), centered around ∼73 Å, indicative of greater structural flexibility and a tendency toward expansion. The difference in PMF profiles

between №1 and №2 underscores the critical role of physiological ionic conditions, particularly the presence of monovalent cations (i.e., Na^+), in maintaining capsid capsid completeness.

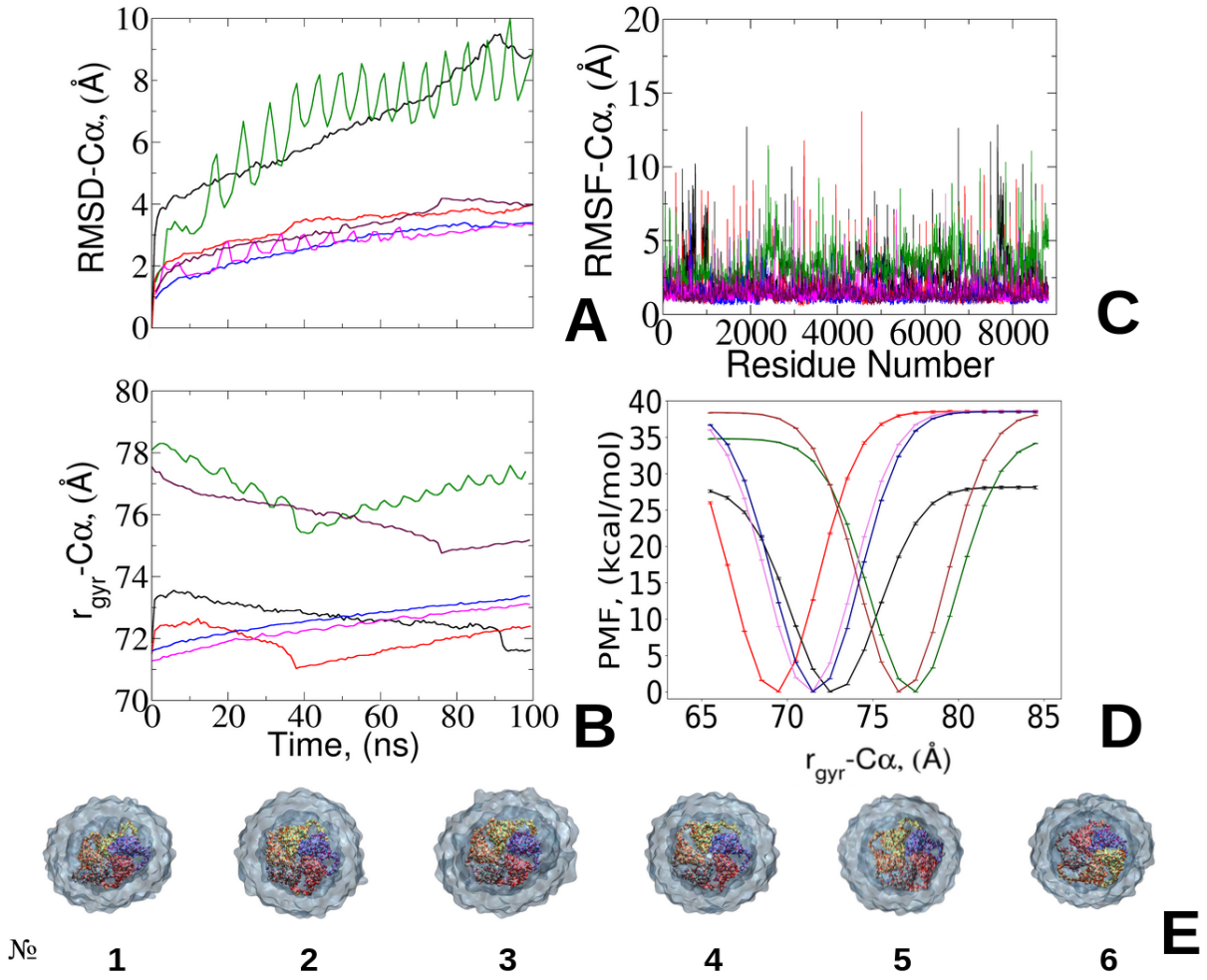

Figure 2. Analysis of structural dynamics of the STMV capsid along MD simulations. (A) Visualization of the capsid highlighting five protomeric subunits (C0–C4) using VMD[42] Surface for protomers and a QuickSurf representation for the entire capsid. Time evolution of the capsid structural properties during a 100-ns conventional MD simulation: (B) Root Mean Square Deviation (RMSD) of Cα atoms and (C) radius of gyration (r_{gyr}) (bottom). (D) Potential of mean force (PMF) plots along the r_{gyr} for the STMV capsid. (E) Root Mean Square Fluctuation (RMSF) of capsid Cα atoms across the different STMV particles. The corresponding colors for each studied viral particles are: №1 - neutralized capsid with Cl^- ions (black), №2 - capsid in physiological NaCl concentration (red), №3 - nucleocapsid in physiological NaCl concentration (green), №4 - nucleocapsid neutralized with $MgCl_2$ (blue), №5 - nucleocapsid in physiological NaCl concentration with Mg^{2+} present (magenta), and №6 - nucleocapsid in 0.5 M NaCl concentration with Mg^{2+} mimicking pH=5 conditions (brown). (F) Final capsid structures obtained from MD simulations under varying conditions.

Among the nucleocapsid-containing particles, structural expansion due to RNA encapsidation and environmental conditions is observed. №3 displays the broadest PMF minimum around 76 Å , reflecting significant structural expansion accompanied by capsid swelling. However, the addition of Mg^{2+} ions shifts the free-energy minimum to a more compact state (e.g., №4, №5), around 71 Å, highlighting the critical role of divalent cations in stabilizing both RNA and the capsid. Interestingly, when the nucleocapsid is neutralized solely with $MgCl_2$ (№4), the resulting distribution spans a broader range of states, similar to №5, suggesting that these environmental conditions may not provide optimal capsid stabilization. In contrast, at pH=5, №6 nucleocapsid maintains a moderately expanded structure near 76 Å while exhibiting enhanced stability, suggesting that ion-mediated shielding of electrostatic forces contributes to preserving capsid integrity even under acidic conditions.

In total, the presented free-energy landscapes reveal the complex role of ions in regulating capsid stability and flexibility. Monovalent ions primarily function is to screen electrostatic interactions and to provide the initial stabilization, while divalent ions contribute to further structural compactness and resilience by neutralizing the RNA and key protein residues, highlighting the differences in the capsid behavior under different ionic conditions.

Water and Ion Flux into the Capsid

In addition to the observed voids (Fig.1C), the simulations reveal the formation of dynamic pores along the capsid, which contributes to the reorganization and increased permeability of solvents and ions at the surface, revealing the STMV sensitivity to environmental changes. To investigate this behavior, we quantified the relative concentration of water molecules and ions within a 5-Å radius of the capsid surface and assessed the flux of these particles across the capsid boundaries. Besides, we analyzed structural transitions by classifying protomer pairs based on their tendency to form stable, tightly packed associations (i.e., occluded protomeric pairs) or dynamic, open interfaces between consecutive protomers (i.e., pore-forming protomeric pairs)(see SI). The details of the methodological setup outlined in the Methods section.

As shown in Fig.3, water and ionic dynamics exhibit both stable and fluctuating behaviors depending on the STMV particle composition. The concentration of water molecules near the capsid surface remains relatively stable across most viral particles, indicating persistent hydration of the capsid interface. Interestingly, the particles of the empty capsid demonstrate an increase in the number of solvent molecules at the interface, whereas nucleocapsids exhibit a net outflow of water, reflecting differing hydration dynamics influenced by the presence of encapsulated RNA. It should be noted that the flux of water molecules, while slow, suggests a dynamic yet gradual exchange of solvent molecules across the capsid boundaries. Thus, the water flux for №3 underwent a noticeable influx toward the end of the simulation, which aligns with the observation of the highest SASA of pore-forming protomer pairs (see Fig.S6, №3), underscoring the structural and dynamic factors that regulate solvent permeability at the capsid interface.

Besides, the relative concentrations and fluxes of ions (Cl^-, Na^+, Mg^{2+}) reveal distinct STMV particle-dependent behaviors. Among the empty capsid STMV particles, the physiological salt concentration tend to stabilize the capsid interface, with Na^+ ions contributing to the solvation shell and modulating Cl^- flux. Thus, №2 shows a high surface concentration of Cl^- ions, but their flux is relatively low, likely due to stable interactions between Na^+ and negatively charged capsid residues. Such behavior contrasts with №1 (neutralized capsid), where the absence of Na^+ leads to a higher Cl^- flux, reflecting the absence of stabilizing counter-ions. The introduction of Mg^{2+} ions further modifies the ionic dynamics, particularly in nucleocapsids. Divalent ions exhibit low flux but establish stable interactions with the capsid, as observed in №4 and №5, where Mg^{2+} remains predominantly localized near the capsid interface. Such stabilization effect contributes to maintaining a moderate hydration level at the interface while reducing the mobility of other ions, including Cl^-. In contrast, the combination of a high concentration of Na^+ and Mg^{2+} in №6 optimizes ionic balance by selectively concentrating both positive ions at the capsid interface, thereby enhancing STMV stability under conditions of lower pH.

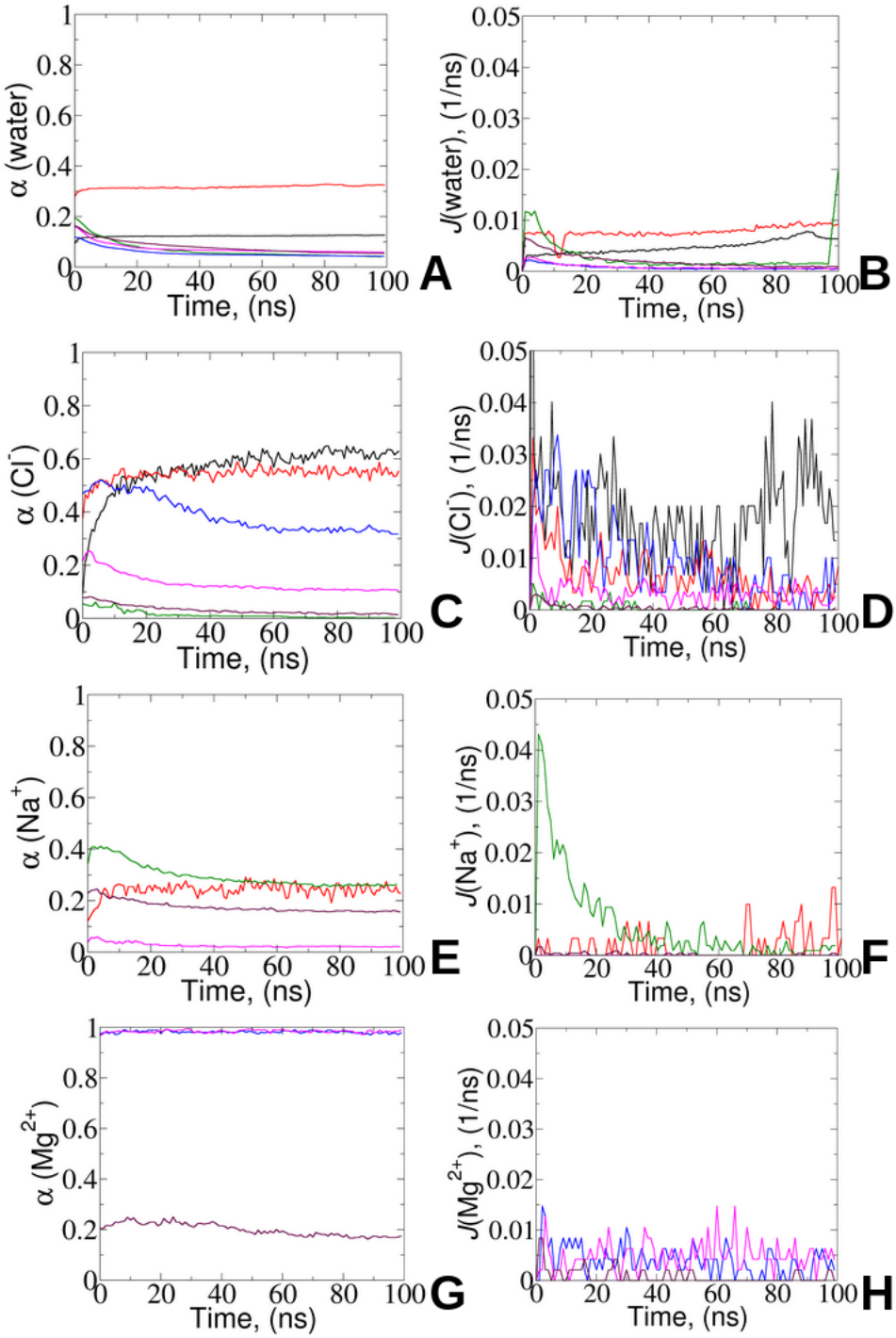

Figure 3. Relative concentration, α, of (A) water molecules, (C) chloride, (E) sodium, and (G) magnesium ions at 5 Å from the capsid surface. Flux through the capsid boundaries along the 100–ns conventional simulation for (B) water molecules, (D) chloride, (F) sodium, and (H) magnesium ions under different conditions: the capsid alone (neutralized with Cl^- ions, black), the capsid alone in physiological NaCl concentration (red), nucleocapsid in physiological NaCl concentration (green), the nucleocapsid neutralized with $MgCl_2$) (blue), the nucleocapsid in physiological NaCl concentration in the presence of Mg^{2+}(magenta), and the nucleocapsid in 0.5M NaCl in the presence of Mg^{2+} (brown).

Residence Time

To better understand the discussed ionic impact, we investigated the preferential ion binding sites and analyzed the residence times of interactions between ions and charged residues of the capsid and RNA. The details of this analysis are provided in the Methods section.

No interactions were observed between Na^+ or Mg^{2+} ions and the capsid residues, indicating that these ions do not directly interfere with interprotomer interactions, which is in line with our observations depicted in Fig.3F, H. Instead, they likely exploit the voids and newly created pores as pathways to access the RNA genome (Fig.4C,D). Interactions between the RNA phosphate groups and Mg^{2+} (Fig.4C) revealed a marked preference for №6, demonstrating the highest proportion of long-residence interactions, reflecting stable and strong binding, which is critical for RNA compaction and nucleocapsid stability. In contrast, №4 and №5, while exhibiting some long-residence interactions, showed a presence of medium- and short-residence interactions with Mg^{2+}, indicating a compensatory mechanism in which the RNA actively engaged with Na^+ ions to stabilize its structure. Such behavior, characterized by transient yet frequent interactions with Na^+ (Fig.4D), reflects the genome ability to adapt to suboptimal ionic conditions by leveraging the available Na^+ ions to counterbalance reduced Mg^{2+} availability or ionic strength, underscoring the dynamic nature of RNA-ion interactions.

The residence time distribution of Cl^- (Fig.4A,B) revealed a dominant short-residence category, indicative of the transient neutralization effect of counter-ions that effectively screens the positive charges on the capsid surface, mitigating electrostatic repulsion and contributing to capsid stabilization. Conversely, interactions with medium- and long-residence times suggest a more persistent blocking effect on capsid positively charged residues (i.e., arginine (ARG) and lysine (LYS)), progressively disrupting interprotomeric ionic interactions, particularly the salt bridges that stabilize the capsid. The disruption of these interactions facilitates the transient stabilization of voids and promotes the formation of new pores at the interprotomeric interfaces, ultimately affecting the overall cohesion and structural integrity of the capsid.

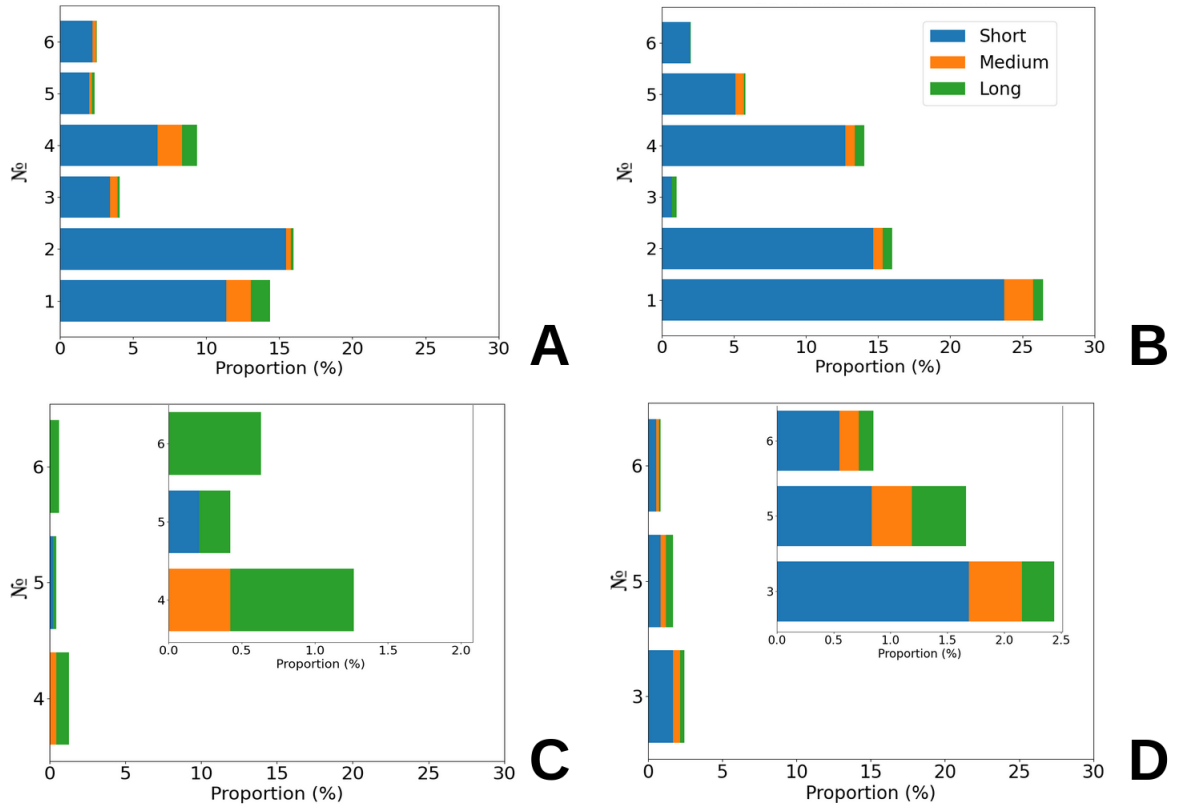

Figure 4. Residence time stacked bar charts for Cl^- ions interacting with charged residues in six different STMV particles. (A) Side-chain ARG interactions with Cl^-. (B) Side-chain LYS interactions with Cl^-. (C) Phosphorus atom of phosphate group of RNA interactions with Mg^{2+} and (D) with Na^+. Bars represent the proportions of residence times categorized as Short (blue, 1–3 ns), Medium (orange, 4–7 ns), and Long (green, >7 ns). STMV particle labels (№1–6) correspond to different simulation conditions, as described in Table 1.

The Role of Ions In Interprotomer Salt-Bridge Disruption

The dynamic interactions of Cl^- with positively charged side chains on the capsid prompted a deeper investigation into the mechanisms driving the modulation of interprotomeric interactions. To address this, we conducted a comprehensive analysis of salt-bridge disruption and examined the role of polarizability in this process, with the №1 serving as a representative example.

Salt-bridge patterns were collected at the initial time point to establish the initial network of interactions (Fig.5A). The heatmap of salt-bridge counts reveals a clear dominance of interprotomeric salt bridges along the diagonal, indicative of strong local interactions stabilizing consecu-

tive protein unit pairs. Besides, a subset of some salt-bridge pairs exhibited four-way salt-bridge interacting patterns, suggesting a higher density of interprotomer salt bridges in these regions (see Table S1 in the SI). A representative example is shown in Fig.5B,C for the subunit pair C4-C5, where salt bridges are formed by donor-acceptor triplets at the initial stages of the simulation: ARG^{C4}_{931}-ASP^{C5}_{15}-ARG^{C4}_{925} and ARG^{C5}_{131}-ASP^{C4}_{815}-ARG^{C5}_{125}.

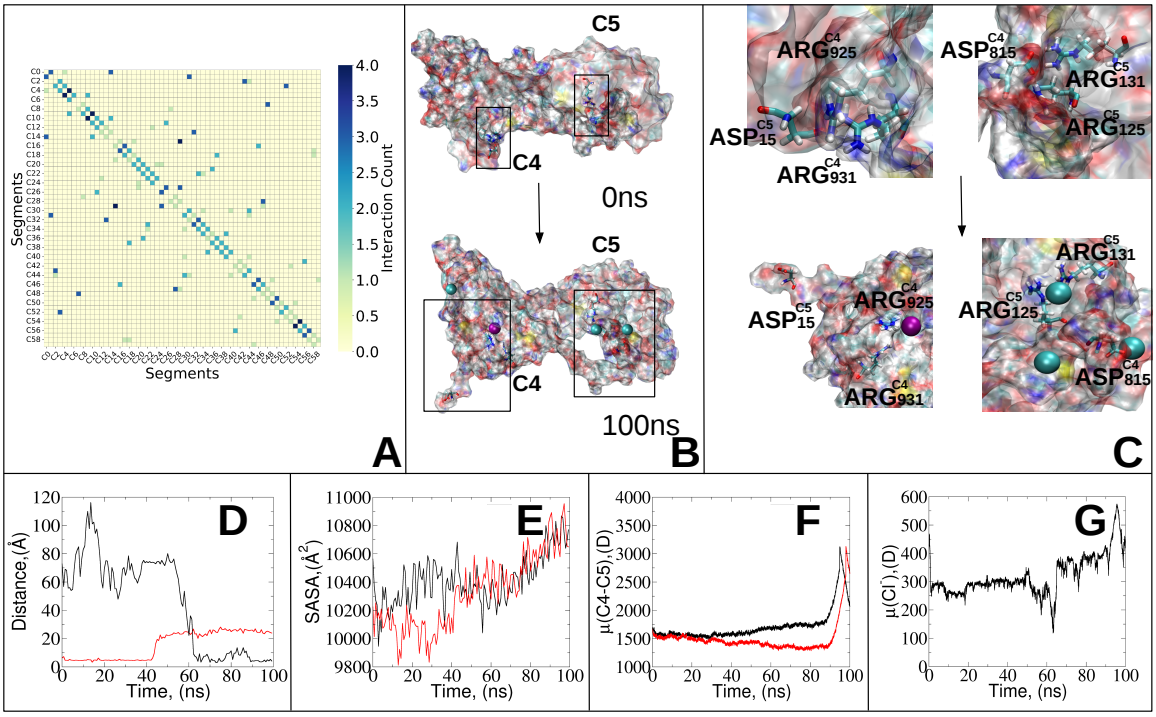

Figure 5. (A) Pattern map of the total number of salt bridges between protomeric pairs. (B) Representation of the disruption of salt bridges between the C4 and C5 protomers, showing the initial capsid configuration (top) and the final simulation frame (bottom). (C) Zoom-in view of the disrupted salt bridges by Cl^- (purple and cyan van der Waals representation) shown in (B). The Cl^- ion shown in purple is described in further detail. (D-G) Temporal analysis of the salt-bridge disruption between C4 and C5 protomers in the neutralized capsid (№1) by Cl^- (purple). (D) Distance between the charged residues (ARG^{C4}_{925} and ASP^{C5}_{15}, red) and the Cl^- ion approaching ARG^{C4}_{925} (black). (E) Dipole moments of the C4 (black) and C5 (red) protomers. (F) Dipole moment of the Cl^- ion. (G) Solvent Accessible Surface Area (SASA) of the C4 (black) and C5 (red) protomers.

Along our simulation, a pore-formation event was observed, in which the interprotomeric salt bridge between the C4-C5 pair was sequentially disrupted, driven by the binding of Cl^- to the positively charged residue at the C4 interface in the neutralized capsid (№1) (Fig.5B,C (bottom)). Structural reorganization and conformational changes within the capsid accompanied this event. By approximately 60 ns (Fig.5D), a Cl^- ion bound to the ARG^{C4}_{925}, reducing its distance to the residue and effectively blocking the positive site at C4. The occurred interaction prevented the salt bridge from reforming, marking a critical step in destabilizing the interprotomeric interaction.

The binding of Cl^- was accompanied by a significant increase in the dipole moment of the Cl^- ion (Fig.5G), reflecting its transition from a solvated state to a direct interaction with the residue. Such disruption also induces structural polarization of the C4 protomer along 60-80 ns (Fig.5F), which was then followed by the rise in their dipole moments due to the progressive solvent exposure (Fig.5E), further highlighting the formation of a transient interprotomeric pore.

It is important to note that all the studied viral particles, except for №6, were analyzed under neutral pH conditions and exhibited identical salt-bridge patterns to this shown in Fig.5A. №6, that mimics the pH=5, showed distinct salt-bridge patterns, which are detailed in Fig.S4 and Table S2 in the SI. Nevertheless, the mechanisms described remain consistent across all studied STMV particles, highlighting the generality of the observed processes.

Conclusions and Perspectives

Leveraging a cumulative of 1-μs polarizable molecular dynamics simulations, our study provides detailed molecular insights into the stability and structural dynamics of the satellite tobacco mosaic virus (STMV) across a spectrum of ionic and pH conditions. By incorporating enhanced sampling along the radius of gyration, we revealed distinct free-energy landscapes that highlight the structural response of its capsid to environmental variations. Shifts in the potential of mean force minima underscored the finely tuned interplay between electrostatic forces and capsid compactness at different stages of the STMV life cycle.

A notable finding of our simulations is the exceptional resilience of the empty STMV capsid to disassembly under physiological conditions. While empty capsids may originate from incomplete assembly processes, their robust stability suggests functional roles in the viral life cycle, potentially reflecting evolutionary adaptations to optimize host interactions while minimizing biosynthetic costs. Notably, the reuse of empty capsids could provide a strategic advantage, allowing the virus to conserve resources by re-encapsulating newly synthesized RNA, especially during co-infection with its helper virus, tobacco mosaic virus (TMV). Such mechanism not only enhances replication efficiency but could also contribute to immune evasion by maintaining structural integrity during host infection. The observed structural stability also highlights the potential of empty capsids as platforms for drug delivery applications. Future investigations into the behavior of other icosahedral viruses could reveal broader evolutionary strategies, offering deeper insights into viral adaptability. Additionally, studying how capsid reuse influences viral infectivity, replication rates, and host immune evasion mechanisms could significantly advance our understanding of virus-host interactions. Simulations of the nucleocapsid under the same physiological conditions revealed a dynamic stage of viral disassembly. The nucleocapsid exhibited near-equilibrium instability, forming a porous, highly permeable structure, likely facilitating efficient RNA release and capsid disassembly. This stage may represent a critical step in the virus replication cycle, where genomic RNA is released and the remaining components are reassembled into new virions.

Our findings also underscore the critical role of ionic interactions in modulating capsid permeability and stability. Mg^{2+} ions stabilize RNA and capsid structures through long-lived interactions with phosphate groups, while Cl^{-} ions regulate salt-bridge disruption and interprotomeric interactions. At pH=5, enhanced cation concentrations (both mono- and divalent) reinforce the nucleocapsid integrity, whereas at pH=7, reduced electrostatic stabilization promotes capsid disassembly, potentially serving as a molecular switch for RNA release. The insights outlined here shed light on how STMV balances stability and adaptability, providing new perspectives on the general mechanisms underlying icosahedral virus structure and function.

Finally, future directions may include the development of antiviral strategies aimed at disrupt-

ing ionic binding to destabilize the capsid, impair viral assembly, or promote premature disassembly. Conversely, mimicking the ionic conditions that stabilize STMV capsids could enable the design of virus-like particles (VLPs) with tailored stability, permeability, and RNA encapsulation properties for applications in drug delivery and controlled-release mechanisms.

Methods

Molecular Dynamics Protocol

Details regarding the composition of the studied STMV particles are provided in Table 1. The initial capsid-related configuration files were obtained from the Urbana Champaign Theoretical and Computational Biophysics Group website[50]. For №6, the capsid protonation at pH=5 was performed using the APBS-PDB2PQR software suite[51], where the PDB 1A34 structure was loaded, and the appropriate protonation states were assigned. Under these conditions, among all charged residues, only GLU_{108} was protonated. The final structure, which included RNA, solvent, and ions, was prepared for further manipulations using the CHARMM-GUI open-source platform[52–54]. The PDB files were then subsequently parameterized with the AMOEBA polarizable force field using the **PDBXYZ** utility available in the TINKER 8 software package[55]. Comprehensive documentation of the TINKER source code can be found in reference 56.

Each system was subjected to an initial energy minimization using the limited-memory Broyden–Fletcher–Goldfarb–Shanno (L-BFGS) algorithm, with the minimization process terminating upon achieving a root mean square (RMS) gradient of 1 kcal/mol. Following satisfactory convergence, the systems were prepared for conventional molecular dynamics (MD) simulations, preliminary pre-equilibrated in NVT ensemble. MD production simulations in the NPT ensemble were then conducted using the BAOAB-RESPA1 integrator[57], implemented within the GPU-accelerated Tinker-HP software package[58,59], which is publicly available through the GitHub repository[60] and the Tinker-HP website[61]. The integration scheme utilized three distinct time steps: a short time step of 0.001 ps for accurately resolving the fastest motions within the system, an intermediate time

step of 0.333 ps to capture medium-frequency motions and interactions efficiently and a 10-fs time step for slowly varying long-range interactions. Given the large size of our systems, exceeding 1 million atoms, each simulation was performed utilizing 8 H100 GPUs, highlighting the exceptional scalability of the Tinker-HP code.

Potential of Mean Force Calculation

To efficiently explore the free-energy landscape of the STMV capsids, we employed well-tempered meta-dynamics (WTMetaD)[37,48,49], an enhanced sampling approach designed to overcome the limitations of conventional MD simulations by dynamically modulating the growth of a bias potential applied to a selected collective variable (CV), thus, preventing overestimation of free-energy barriers and ensuring smooth convergence of the free-energy surface. WTMetaD scales the bias height based on the accumulated bias energy, ensuring that the system remains close to thermodynamic equilibrium, preserving realistic pathways during sampling. For the potential of mean force (PMF) calculation, given the large-scale nature of capsid dynamics, we selected the radius of gyration (r_{gyr}) as the CV. The choice of r_{gyr} was informed by an initial analysis of conventional MD simulations, where we observed its gradual increase over time without reaching a plateau, making it an effective descriptor of the capsid global structural changes. For the WTMetaD calculations along r_{gyr} we used the C_α atoms of the capsid, as implemented in the Colvars Module[62–64] in combination with the Tinker-HP software. To ensure accurate and reproducible results, all PMF calculations were performed in four replicas for each STMV particle, providing robust statistical averaging and minimizing the risk of biases or inconsistencies in the free-energy estimates. In total, 300 ns of accumulated time (12.5 ns per replica) was simulated.

Root Mean Square Deviation

The Root Mean Square Deviation (RMSD) analysis was conducted using the VMD software[42]. To accurately quantify structural deviations over time, the capside backbone atoms were aligned to a reference structure extracted from the initial timeframe. This alignment step removes any trans-

lational and rotational movements that do not reflect genuine conformational changes, allowing for a more precise comparison of the structural evolution. Following alignment, the RMSD of the backbone was calculated across all simulation frames. This provided insights into how much the structure deviated from the reference over time, indicating the overall stability of the capsid in the various environmental conditions. The results were then plotted to visualize the trends in structural stability.

Root Mean Square Fluctuation

The Root Mean Square Fluctuation (RMSF) of protein C_α atoms was computed to assess the dynamic behavior of the SARS-CoV-2 spike protein. Utilizing the Visual Molecular Dynamics (VMD) software package[42], the total number of frames in the molecular system was determined. The RMSF calculation was then performed using the **measure rmsf** utility available in VMD, which generated RMSF values for each C_α atom over the trajectory frames.

Capsid-RNA Hydrogen Bonding Analysis

To examine the hydrogen bond interactions within nucleotide-present STMV assemblies under varying environmental conditions, we analyzed hydrogen-bond data derived from the trajectory in VMD[42]. Using a distance criterion of 9 Å and an angle threshold of 90° for evaluating protein-RNA hydrogen bonding[65–68], we assessed RNA-capsid interactions across nucleocapsid-related STMV particles (№3-№6, Table 1). The total number of hydrogen bonds for each interaction type was extracted for each nanosecond of the trajectory.

To compare the hydrogen bond distributions, we calculated the percentage contribution of each interaction type to the total hydrogen bond count for each system. This approach allowed us to assess the relative abundance of different hydrogen-bond types, independent of system size. The interaction types were visualized in scatter plots, with each system represented on the x-axis and the hydrogen bond percentage on the y-axis.

Interprotomeric Salt-Bridges Analysis

To investigate the salt-bridge interactions between protomers in the STMV capsid, we first identified the initial salt-bridge patterns from the initial frame of molecular dynamics simulations using VMD. This initial dataset was used as a reference for subsequent analysis. The extracted patterns were systematically processed to identify residue pairs forming interprotomeric salt bridges, focusing on interactions involving segments labeled from C0 to C59.

The data were parsed and grouped by amino acid pairs and corresponding segment interactions. Interaction counts were calculated, excluding self-interactions and ensuring symmetry in the segment pair ordering. These counts were then organized into a matrix representing the frequency of salt-bridge formation between segment pairs.

To visualize the interprotomeric salt-bridge network, a heatmap was constructed, illustrating the interaction density between segments. The heatmap highlighted regions of high interaction frequency, providing insights into the structural organization and stability of the capsid. Variations in the interaction patterns under different conditions were further analyzed to assess the role of ionic interactions in capsid structural integrity.

Relative Hydration and Ionic 5–Å Shell Concentration

To investigate the dynamics of the capsid hydration and ionic shell, we tracked the number of water molecules and ions located within 5 Å of the capsid surface at each frame of the MD trajectory. To enable the comparison among systems with different ionic strengths and varying total ions/water molecules counts, we normalized the count of ions/water molecules within this 5-Å region by their total number in the system at each frame, yielding a dimensionless ratio that reflects local concentration, α, independently of system size.

Radius of Gyration

To calculate the radius of gyration (r_{gyr}) for the capsid, VMD[42] was first used to extract the Cα atom coordinates from all frames of the simulation. These coordinates were then processed in Colvars Dashboard plugin[69] available in VMD.

Water and Ionic Flux Across the Capsid

To accurately determine how many water molecules or ions permeate through the capsid (i.e., flux), for each frame of the simulation, the positions of all water molecules/ions were recorded. Based on their positions relative to the capsid boundary, we classify them as either inside or outside the capsid. This classification is done using the distance from water molecules/ions to the center of the capsid compared to the capsid radius. Water molecules/ions that were outside the capsid in the previous frame but are found inside the capsid in the current frame are considered to have crossed the boundary inward (i.e., influx). Conversely, water molecules/ions that were inside the capsid in the previous frame but were found outside the capsid in the current frame are considered to have crossed the boundary outward (i.e., efflux). The total particle flux, J for each frame is calculated by summing the influx and efflux counts. Since the MD simulation provides the trajectory data at discrete time intervals, the flux is computed as the rate of crossing events per unit time:

$$J = \frac{N_{\text{influx}} + N_{\text{efflux}}}{N_{\text{tot}} \Delta t} \tag{1}$$

Here, N_{influx} and N_{efflux} are the numbers of water molecules/ions crossing the capsid boundary inward and outward, respectively, N_{tot} correspond to the total number of water molecules/ions in the simulation box, and Δt is the time difference between consecutive frames.

K-means Clustering

To investigate the capsid porosity, we analyzed the relationship between the center-of-mass (COM) distance and the solvent-accessible surface area (SASA) for protomeric pairs within the capsid.

The COM distances were computed using a TCL script in VMD, which calculated the Euclidean distance (via the **vecdist** function) between the COM of each consecutive segment. Similarly, SASA values were determined using a TCL script in VMD, employing **measure sasa** with a probe radius of 1.4 Å to calculate the SASA for each pair. Both COM distance and SASA data were accumulated across all frames of the trajectory. The average and standard deviation for both variables were then computed for each protomeric pair.

To identify meaningful groupings of molecular pairs, K-means clustering was applied to the processed data, with the number of clusters set to four ($k = 4$). The clustering algorithm used both SASA and distance as features, with the aim of partitioning the data into distinct groups based on these properties. Following the clustering, the cluster with the smallest average SASA was identified as the cluster of "occluded protomer pairs," while the cluster with the largest average SASA was considered the "pore-forming protomer pairs". These clusters were extracted for detailed analysis. To illustrate the clustering results, a combined scatter plot by means of the matplotlib python library[70] was generated, displaying SASA against COM distance for molecular pairs in both the smallest and largest clusters. Error bars were included to represent the standard deviations of SASA and COM distance, providing insights into the variability of the data. The plot was color-coded, with the occluded pairs cluster represented in blue and the pore-forming cluster in green.

Ion-Residue Residence Time Analysis

To investigate the dynamics of ion interactions with specific molecular groups, we quantified the residence times of ions near target residues using a TCL script in VMD, employing **measure contacts** within a defined cutoff distance along the trajectory. The cutoff distances used for detecting interactions were derived from the first peak of the radial distribution function (RDF) for each pair of ion and a charged group of a residue side-chain pair, such as LYS (3.2 Å) and ARG (3.4 Å) interacting with Cl^- and phosphorus atom of phosphodiester of RNA interacting with Mg^{2+} (3.2 Å) and Na^+ (3.5 Å) (see Fig.S3 in SI). The residence time for each ion was calculated as the cumula-

tive number of nanoseconds in which the ion remained within the interaction cutoff distance. This allowed for a detailed analysis of ion dynamics, focusing on their short-range interactions.

Building on this analysis, we further grouped the residence time data into three categories—short (1–3 ns), medium (4–7 ns), and long (>7 ns)—to facilitate the interpretation of interaction durations. The total number of ions was used to normalize the residence time counts, allowing meaningful comparisons across systems with varying ion concentrations. The results were visualized using horizontal stacked bar chart plots, where each bar represented the distribution of residence times for a given STMV particle, residue, and ion type, therefore, highlighting the relative prevalence of short-, medium-, and long-term interactions, providing a clear and comparative view of interaction lifetimes.

Acknowledgments

This work has received funding from the European Research Council (ERC) under the European Union's Horizon 2020 research and innovation program (grant agreement No 810367), project EMC2 (JPP). ZV thanks the National Science Foundation (NSF) for funding her research stay (grant CHE-2244028). Computations have been performed at IDRIS (Jean Zay) on GENCI Grants: no A0150712052 (J.-P. P.) and grant GC010815453 (Grand Challenge H100 Jean Zay, J.-P. P.)

Data availability

Unless otherwise stated, all data supporting the results of this study can be found in the article or supplementary information.

Code availability

MD simulations were performed using the Tinker-HP v1.2: https://github.com/TinkerTools/tinker-hp

Author contribution

Designed research: M. B., L. L., J.-P. P. ; **Performed research:** M. B. , Z. V.; **Contributed analytic tools:** O.A ., L. L., J.-P. P.; **Analysis:** M. B., L. L., J.-P. P. ; **Wrote the paper:** M. B., J.-P. P. with the inputs of all authors.

Conflict of interest/Competing interests

L. L., and J.-P. P. are co-founders and shareholders of Qubit Pharmaceuticals. The remaining authors declare no competing interests.

Materials & Correspondence

Correspondence and requests for materials should be addressed to Marharyta Blazhynska or Jean-Philip Piquemal.

References

(1) Mirkov, T. E.; Mathews, D. M.; Du Plessis, D. H.; Dodds, J. A. Nucleotide sequence and translation of satellite tobacco mosaic virus RNA. *Virology* **1989**, *170*, 139–146.

(2) Dodds, J. A. Satelite tobacco mosaic virus. *Annu. Rev. Phytopathol.* **1998**, *36*, 295–310.

(3) Valverde, R. A.; Dodds, J. A. Evidence for a satellite RNA associated naturally with the U5 strain and experimentally with the U1 strain of tobacco mosaic virus. *J. Virol.* **1986**, *67*, 1875–1884.

(4) Valverde, R. A.; Dodds, J. A. Some properties of isometric virus particles which contain the satellite RNA of tobacco mosaic virus. *J. Gen. Virol.* **1987**, *68*, 965–972.

(5) Larson, S. B.; Koszelak, S.; Day, J.; Greenwood, A.; Dodds, J. A.; McPherson, A. 3-Dimensional structure of satellite tobacco mosaic virus at 2.9 Angstrom resolution. *J. Mol. Biol.* **1993**, *231*, 375–391.

(6) Larson, S. B.; Koszelak, S.; Day, J.; Greenwood, A.; Dodds, J. A.; McPherson, A. Double-helical RNA in satellite tobacco mosaic virus. *Nature* **1993**, *361*, 179–182.

(7) Kuznetsov, Y. G.; Larson, S. B.; Day, J.; Greenwood, A.; McPherson, A. Structural transitions of satellite tobacco mosaic virus particles. *Virology* **2001**, *284*, 223–234.

(8) Adolph, K.; Butler, P. Studies on the assembly of a spherical plant virus: I. States of aggregation of the isolated protein. *J. Mol. Biol.* **1974**, *88*, 327–341.

(9) Johnson, J. E.; Speir, J. A. Quasi-equivalent viruses: a paradigm for protein assemblies. *J. Mol. Biol.* **1997**, *269*, 665–675.

(10) Ni, P.; Cheng Kao, C. Non-encapsidation activities of the capsid proteins of positive-strand RNA viruses. *Virology* **2013**, *446*, 123–132.

(11) Tsao, J.; Chapman, M.; Agbandje, M.; Keller, W.; Smith, K.; Wu, H.; Luo, M.; Smith, T.; Rossmann, M.; Compans, R. The three-dimensional structure of canine parvovirus and its functional implications. *Science* **1991**, *251*, 1456–1464.

(12) Fisher, A.; Johnson, J. Ordered duplex RNA controls capsid architecture in an icosahedral animal virus. *Nature* **1993**, *361*, 176–179.

(13) McKenna, R.; Xia, D.; Willingmann, P.; others Atomic structure of single-stranded DNA bacteriophage ΦX174 and its functional implications. *Nature* **1992**, *355*, 137–143.

(14) Erickson, J.; Silva, A.; Murthy, M.; Fita, I.; Rossmann, M. The structure of a T = 1 icosahedral empty particle from southern bean mosaic virus. *Science* **1985**, *229*, 625–629.

(15) Chen, Z. G.; Stauffacher, C.; Li, Y.; others Protein-RNA interactions in an icosahedral virus at 3.0 Å resolution. *Science* **1989**, *245*, 154–159.

(16) Zlotnick, A.; Aldrich, R.; Johnson, J. M.; Ceres, P.; Young, M. J. Mechanism of capsid assembly for an icosahedral plant virus. *Virology* **2000**, *277*, 450–456.

(17) Johnson, J. M.; others Regulating self-assembly of spherical oligomers. *Nano Lett.* **2005**, *5*, 765–770.

(18) Sivanandam, V.; Mathews, D.; Garmann, R.; others Functional analysis of the N-terminal basic motif of a eukaryotic satellite RNA virus capsid protein in replication and packaging. *Sci. Rep.* **2016**, *6*, 26328.

(19) Wolstenholme, G. E. W., O'Connor, M., Eds. *Strategy of the Viral Genome*; Wiley: Hoboken, NJ, 2009; p 192, E-book format, published on September 16, 2009.

(20) Baker, T. S.; Newcomb, W. W.; Booy, F. P.; Brown, J. C.; Steven, A. C. Three-dimensional structures of maturable and abortive capsids of equine herpesvirus 1 from cryoelectron microscopy. *J. Virol.* **1990**, *64*, 563–573.

(21) Freddolino, P. L.; Arkhipov, A. S.; Larson, S. B.; McPherson, A.; Schulten, K. Molecular Dynamics Simulations of the Complete Satellite Tobacco Mosaic Virus. *Structure* **2006**, *14*, 437–449.

(22) Arkhipov, A.; Freddolino, P. L.; Schulten, K. Stability and dynamics of virus capsids described by coarse-grained modeling. *Structure* **2006**, *14*, 1767–1777.

(23) Shi, Y.; Xia, Z.; Zhang, J.; Best, R.; Wu, C.; Ponder, J. W.; Ren, P. Polarizable Atomic Multipole-Based AMOEBA Force Field for Proteins. *J. Chem. Theory Comput.* **2013**, *9*, 4046–4063.

(24) Ponder, J. W.; Wu, C.; Ren, P.; Pande, V. S.; Chodera, J. D.; Schnieders, M. J.; Haque, I.; Mobley, D. L.; Lambrecht, D. S.; DiStasio, R. A.; Head-Gordon, M.; Clark, G. N. I.; Johnson, M. E.; Head-Gordon, T. Current Status of the AMOEBA Polarizable Force Field. *J. Phys. Chem. B* **2010**, *114*, 2549–2564.

(25) Zhang, C.; Lu, C.; Jing, Z.; Wu, C.; Piquemal, J.-P.; Ponder, J. W.; Ren, P. AMOEBA Polarizable Atomic Multipole Force Field for Nucleic Acids. *J. Chem. Theory Comput.* **2018**, *14*, 2084–2108.

(26) Frank, J. A.; Feschotte, C. Co-option of endogenous viral sequences for host cell function. *Curr. Opin. Virol.* **2017**, *25*, 81–89.

(27) Weis, F.; Beckers, M.; von der Hocht, I.; Sachse, C. Elucidation of the viral disassembly switch of tobacco mosaic virus. *EMBO Rep.* **2019**, *20*, e48451.

(28) Caspar, D. Assembly and Stability of the Tobacco Mosaic Virus Particle. *Adv. Protein Chem.* **1964**, *18*, 37–121.

(29) Klug, A.; Caspar, D. L. The structure of small viruses. *Adv. Virus Res.* **1960**, *7*, 225–325.

(30) Staring, J.; Raaben, M.; Brummelkamp, T. R. Viral escape from endosomes and host detection at a glance. *J. Cell Sci.* **2018**, *131*, jcs216259.

(31) Patarroyo, C.; Laliberté, J.-F.; Zheng, H. Hijack it, change it: how do plant viruses utilize the host secretory pathway for efficient viral replication and spread? *Front. Plant Sci.* **2013**, *3*.

(32) Bancroft, J. B. The self-assembly of spherical plant viruses. *Adv. Virus Res.* **1970**, *16*, 99–134.

(33) Kurtz-Fritsch, C.; Hirth, L. Uncoating of two spherical plant viruses. *Virology* **1972**, *47*, 385–396.

(34) Wennerström, H.; Oliveberg, M. On the osmotic pressure of cells. *QRB Discov.* **2022**, *3*, e12.

(35) Bowman, J. C.; Lenz, T. K.; Hud, N. V.; Williams, L. D. Cations in charge: magnesium ions in RNA folding and catalysis. *Curr. Opin. Struct. Biol.* **2012**, *22*, 262–272.

(36) Brännvall, M.; Kirsebom, L. A. Metal ion cooperativity in ribozyme cleavage of RNA. *Proc. Natl. Acad. Sci. U. S. A.* **2001**, *98*, 12943–12947.

(37) Barducci, A.; Bussi, G.; Parrinello, M. Well-Tempered Metadynamics: A Smoothly Converging and Tunable Free-Energy Method. *Phys. Rev. Lett.* **2008**, *100*, 020603.

(38) Speir, J. A.; Munshi, S.; Wang, G.; Baker, T. S.; Johnson, J. E. Structures of the native and swollen forms of cowpea chlorotic mottle virus determined by X-ray crystallography and cryo-electron microscopy. *Struct.* **1995**, *3*, 63–78.

(39) Kagra, D.; Jangra, R.; Sharma, P. Exploring the Nature of Hydrogen Bonding between RNA and Proteins: A Comprehensive Analysis of RNA:Protein Complexes. *ChemPhysChem* **2022**, *23*, e202100731.

(40) Ohri, A.; Seelam, P. P.; Sharma, P. A quantum chemical view of the interaction of RNA nucleobases and base pairs with the side chains of polar amino acids. *J. Biomol. Struct. Dyn.* **2020**, *39*, 5411–5426.

(41) Kagra, D.; Prabhakar, P. S.; Sharma, K. D.; Sharma, P. Structural Patterns and Stabilities of Hydrogen-Bonded Pairs Involving Ribonucleotide Bases and Arginine, Glutamic Acid, or Glutamine Residues of Proteins from Quantum Mechanical Calculations. *ACS Omega* **2020**, *5*, 3612–3623.

(42) Humphrey, W.; Dalke, A.; Schulten, K. VMD – Visual Molecular Dynamics. *J. Mol. Graph.* **1996**, *14*, 33–38.

(43) Sanner, M. F.; Olson, A. J.; Spehner, J.-C. Reduced surface: an efficient way to compute molecular surfaces. *Biopolymers* **1996**, *38*, 305–320.

(44) Misra, V. K.; Draper, D. E. On the role of magnesium ions in RNA stability. *Biopolymers* **1998**, *48*, 113–135.

(45) Draper, D. E. A guide to ions and RNA structure. *RNA* **2004**, *10*, 335–343.

(46) Shaw, A. B.; Tse, H. N.; Byford, O.; Plahe, G.; Moon-Walker, A.; Hover, S. E.; Saphire, E. O.;

Whelan, S. P. J.; Mankouri, J.; Fontana, J.; Barr, J. N. Cellular endosomal potassium ion flux regulates arenavirus uncoating during virus entry. *mBio* **2024**, *15*, e01684–23.

(47) Hargest, V.; Davis, A.; Schultz-Cherry, S. In *Encyclopedia of Virology (Fourth Edition)*, fourth edition ed.; Bamford, D. H., Zuckerman, M., Eds.; Academic Press: Oxford, 2021; pp 92–99.

(48) Laio, A.; Parrinello, M. Escaping Free-Energy Minima. *Proc. Natl. Acad. Sci. U.S.A.* **2002**, *99*, 12562–12566.

(49) Dama, J. F.; Parrinello, M.; Voth, G. A. Well-Tempered Metadynamics Converges Asymptotically. *Phys. Rev. Lett.* **2014**, *112*, 240602.

(50) Theoretical and Computational Biophysics Group, University of Illinois at Urbana-Champaign NAMD Utilities. https://www.ks.uiuc.edu/Research/namd/utilities/stmv/, 2024; Accessed: 2024-11-20.

(51) Jurrus, E. et al. Improvements to the APBS biomolecular solvation software suite. *Protein Sci.* **2018**, *27*, 112–128.

(52) Park, S. J.; Kern, N. R.; Brown, T.; Lee, J.; Im, W. CHARMM-GUI PDB Manipulator: Various PDB Structural Modifications for Biomolecular Modeling and Simulation. *J. Mol. Biol.* **2023**, *167995*, Preprint.

(53) Jo, S.; Kim, T.; Iyer, V. G.; Im, W. CHARMM-GUI: A Web-based Graphical User Interface for CHARMM. *J. Comput. Chem.* **2008**, *29*, 1859–1865.

(54) Jo, S.; Cheng, X.; Islam, S. M.; Huang, L.; Rui, H.; Zhu, A.; Lee, H. S.; Qi, Y.; Han, W.; Vanommeslaeghe, K.; MacKerell, J., A. D.; Roux, B.; Im, W. CHARMM-GUI PDB Manipulator for Advanced Modeling and Simulations of Proteins Containing Non-standard Residues. *Adv. Protein Chem. Struct. Biol.* **2014**, *96*, 235–265.

(55) Rackers, J. A.; Wang, Z.; Lu, C.; Laury, M. L.; Lagardère, L.; Schnieders, M. J.; Piquemal, J.-P.; Ren, P.; Ponder, J. W. Tinker 8: Software Tools for Molecular Design. *J. Chem. Theory Comput.* **2018**, *14*, 5273–5289.

(56) Tinker Guide- Tinker Molecular Modeling Package. https://dasher.wustl.edu/tinker/distribution/doc/tinker-guide.pdf.

(57) Lagardère, L.; Aviat, F.; Piquemal, J.-P. Pushing the Limits of Multiple-Time-Step Strategies for Polarizable Point Dipole Molecular Dynamics. *J. Phys. Chem. Lett.* **2019**, *10*, 2593–2599.

(58) Lagardère, L.; Jolly, L.-H.; Lipparini, F.; Aviat, F.; Stamm, B.; Jing, Z. F.; Harger, M.; Torabifard, H.; Cisneros, G. A.; Schnieders, M. J.; Gresh, N.; Maday, Y.; Ren, P. Y.; Ponder, J. W.; Piquemal, J.-P. Tinker-HP: a massively parallel molecular dynamics package for multiscale simulations of large complex systems with advanced point dipole polarizable force fields. *Chem. Sci.* **2018**, *9*, 956–972.

(59) Adjoua, O.; Lagardère, L.; Jolly, L.-H.; Durocher, A.; Very, T.; Dupays, I.; Wang, Z.; Inizan, T. J.; Célerse, F.; Ren, P.; Ponder, J. W.; Piquemal, J.-P. Tinker-HP: Accelerating Molecular Dynamics Simulations of Large Complex Systems with Advanced Point Dipole Polarizable Force Fields Using GPUs and Multi-GPU Systems. *J. Chem. Theory Comput.* **2021**, *17*, 2034–2053.

(60) Adjoua, O. Tinker-HP: High-Performance Massively Parallel Evolution of Tinker on CPUs & GPUs. https://github.com/TinkerTools/Tinker-HP.

(61) Piquemal, J.-P.; Lagardère, L.; Adjoua, O.; Jolly, L.-H. Tinker-HP: High-Performance Massively Parallel Evolution of Tinker on CPUs & GPUs. https://tinker-hp.org/.

(62) Hénin, J.; Fiorin, G.; Chipot, C.; Klein, M. L. Exploring Multidimensional Free Energy Landscapes Using Time-Dependent Biases on Collective Variables. *J. Chem. Theory Comput.* **2010**, *6*, 35–47.

(63) Fiorin, G.; Klein, M. L.; Hénin, J. Using Collective Variables to Drive Molecular Dynamics Simulations. *Mol. Phys.* **2013**, *111*, 3345–3362.

(64) Fiorin, G.; Marinelli, F.; Forrest, L. R.; others Expanded Functionality and Portability for the Colvars Library. *J. Phys. Chem. B* **2024**, *128*, 11108–11123.

(65) Morozova, N.; Allers, J.; Myers, J.; Shamoo, Y. Protein–RNA interactions: exploring binding patterns with a three-dimensional superposition analysis of high resolution structures. *Bioinformatics* **2006**, *22*, 2746–2752.

(66) Kim, H.; Jeong, E.; Lee, S. W.; Han, K. Computational analysis of hydrogen bonds in protein–RNA complexes for interaction patterns. *FEBS Lett.* **2003**, *552*, 231–239.

(67) Bahadur, R. P.; Zacharias, M.; Janin, J. Dissecting protein–RNA recognition sites. *Nucleic Acids Res.* **2008**, *36*, 2705–2716.

(68) Barik, S.; Pilla, P. P.; Bahadur, R. P. Molecular architecture of protein-RNA recognition sites. *J. Biomol. Struct. Dyn.* **2015**, *33*, 2738–2751.

(69) Hénin, J.; Lopes, L. J. S.; Fiorin, G. Human learning for molecular simulations: the Collective Variables Dashboard in VMD. *J. Chem. Theory Comput.* **2022**, *18*, 1945–1956.

(70) Hunter, J. D. Matplotlib: A 2D graphics environment. *Comput. Sci. Eng.* **2007**, *9*, 90–95.